Influence of Sr-Site Deficiency, Ca/Ba/La Doping on the Exsolution of Ni from SrTiO$_3$

Willis O'Leary, Livia Giordano, Jieun Park, Stephen S. Nonnenmann, Yang Shao-Horn, and Jennifer L. M. Rupp*

Cite This: https://doi.org/10.1021/jacs.2c12011

Read Online

ACCESS | Metrics & More | Article Recommendations | Supporting Information

ABSTRACT: Cermet catalysts formed via exsolution of metal nanoparticles from perovskites promise to perform better in electro- and thermochemical applications than those synthesized by conventional wet-chemical approaches. However, a shortage of robust material design principles still stands in the way of widespread commercial adoption of exsolution. Working with Ni-doped SrTiO$_3$ solid solutions, we investigated how the introduction of Sr deficiency as well as Ca, Ba, and La doping on the Sr site changed the size and surface density of exsolved Ni nanoparticles. We carried out exsolution on 11 different compositions under fixed conditions. We elucidated the effect of A-site defect size/valence on nanoparticle density and size as well as the effect of composition on nanoparticle immersion and ceramic microstructure. Based on our experimental results, we developed a model that quantitatively predicted a composition's exsolution properties using density functional theory calculations. The model and calculations provide insights into the exsolution mechanism and can be used to find new compositions with high exsolution nanoparticle density.
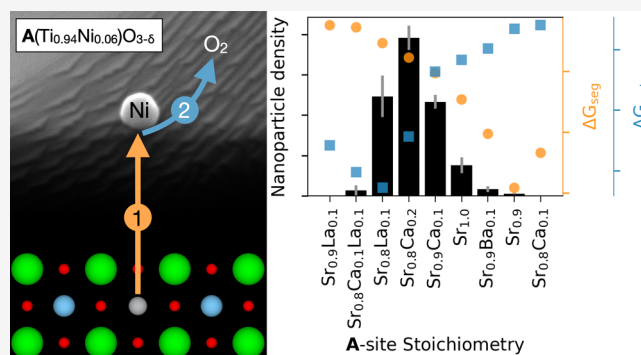
1. INTRODUCTION

Nanoparticle (NP)-decorated ceramics are used in a wide assortment of chemical and energy conversion applications.[1] Most existing materials are made by deposition of metal NPs on ceramic surfaces, for example, by infiltration and reduction of an aqueous metal salt. This yields a metal–ceramic composite, or cermet for short. However, metal–ceramic interfaces created through deposition are relatively weak, allowing for NP agglomeration,[1] and provide little protection against coking in carbon-rich environments.[2] As a result, conventional cermets degrade quickly, requiring costly reactivation or replacement.

To solve these problems, an alternative synthetic route to cermets has been proposed: exsolution. Here, a perovskite is reduced at high temperatures, which drives exsolution of transition-metal B-site cations from the ABO$_{3-\delta}$ structure to form catalytically active metal NPs on the surfaces (Figure 1a,b). Exsolved metal NPs are partially immersed in the perovskite, giving them uniquely high resistance to agglomeration and coking.[3,4] In some materials, such as precious-metal-doped LaFeO$_3$, exsolution is highly reversible, which can improve the stability of catalysts operating in both reducing and oxidizing environments.[5] Over the past two decades, these advantages have driven the development of a diverse range of exsolution cermets for a multitude of applications, including solid oxide fuel cells,[6] steam electrolysis,[7] thermochemical
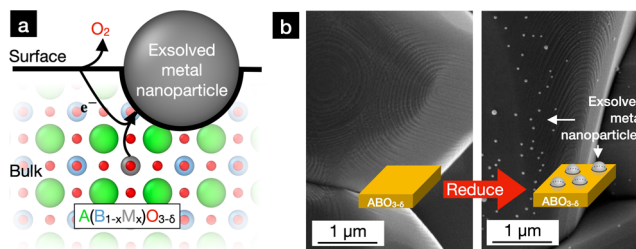

Figure 1. (a) Schematic of exsolution from a generic perovskite with formula A(B$_{1-x}$M$_x$)O$_{3-\delta}$. Under a reducing atmosphere, oxyegn leaves the lattice and metal (M) cations combine with compensating electrons to form metal nanoparticles on the material surface. (b) Representative result of exsolution processing on a Sr$_{0.8}$La$_{0.1}$Ti$_{0.94}$Ni$_{0.06}$O$_{3-\delta}$ pellet observed via SEM.

cycling,[8] and dry methane reforming.[9] However, despite great strides highlighted in recent reviews,[10,11] a shortage of robust

Table 1. Survey of Studies with Significant Emphasis on Tuning Exsolution[a]

design parameters	tuned nanoparticle properties	underlying perovskite properties	study type[b]	A	B (exsolved)	refs
titanates						
A-site composition	density	surface morphology	e	$La_{0.3}Sr_{0.7}$	$Ti_{0.94}Ni_{0.06}$	12
B-site composition		A-site surface segregation		$La_{0.8}Ce_{0.1}$	$Ti_{0.6}Ni_{0.4}$	
fracture		phase stability		$La_{.64-.06m}Sr_{.16+.06m}$	$Ti_{0.94}Fe_{0.06}$	
				$La_{.64-.06m}Sr_{.16+.06m}$	$Ti_{0.94}Ni_{0.06}$	
				$La_{0.4}Sr_{0.4}$	$Ti_{0.94}Mn_{0.06}$	
				$La_{0.4}Sr_{0.4}$	$Ti_{0.94}Fe_{0.06}$	
				$La_{0.4}Sr_{0.4}$	$Ti_{0.94}Ni_{0.06}$	
				$La_{0.4}Sr_{0.4}$	$Ti_{0.94}Co_{0.06}$	
A-site composition	immersion	surface orientation	e	$La_{0.4}Sr_{0.4}$	$Ti_{0.97}Ni_{0.03}$	13
reduction temperature	stability	A-site surface segregation		$La_{0.52}Sr_{0.28}$	$Ti_{0.94}Ni_{0.06}$	
		cation diffusion				
		surface restructuring				
		surface roughness				
B-site composition	size	phase stability	e	$La_{0.4}Sr_{0.4}$	$Ti_{0.94}Ni_{0.06}$	7
	density	O deficiency			$Ti_{0.94}Fe_{0.06}$	
		B-site dopant size				
		B-site reducibility				
substrate/film lattice mismatch	density	strain	e, m	$La_{0.2}Sr_{0.7}$	$Ti_{0.9}Ni_{0.1}$	14
	size	strain relaxation energy				
substrate orientation	density	surface orientation	e, m	$La_{0.2}Sr_{0.7}$	$Ti_{0.9}Ni_{0.1}$	15
	size	strain				
	immersion	metal/oxide interfacial energy				
reduction temperature	size	oxygen transport	e	$La_{0.5}Ca_{0.4}$	$Ti_{0.8}Ni_{0.2}$	16
reducing gas						
reduction temperature	density		e	$La_{0.2}Sr_{0.7}$	$Ti_{0.9}Ni_{0.1}$	17
reduction time	size					
reduction temperature	size		e	$La_{0.43}Ca_{0.37}$	$Ti_{1-x}Rh_x$	18
reduction time	density					
B-site composition	total volume					
reduction temperature	size		e	$La_{0.43}Ca_{0.37}$	$Ti_{0.94}Rh_{0.06}$	19
reduction time	width	concentration of exsolveable ions	e, m	$La_{0.43}Ca_{0.37}$	$Ti_{0.94}Ni_{0.06}$	3
reducing gas	height	strain		$La_{0.8}Ce_{0.1}$	$Ti_{0.6}Ni_{0.4}$	
	shape	cation diffusion				
A-site composition	density	B-site surface segregation	e, d	Sr	$Ti_{0.9}Ni_{0.1}$	20
		surface orientation		$Sr_{0.8}$		
		surface termination		$La_{0.1}Sr_{0.9}$		
				$La_{0.08}Sr_{0.72}$		
B-site composition	density	nucleation activation energy	e, m	$La_{0.3}Sr_{0.5}$	$Ti_{1-x}Ni_x$	21
A-site composition	size	growth activation energy		$La_{0.3}Ce_{0.04}Sr_{0.46}$		
ferrites						
calcination temperature	exsolveability	B-site surface segregation	d	La	$Fe_{1-x}Pt_x$	22
		surface termination				
calcination temperature	exsolveability	Pt surface segregation	d	La	$Fe_{1-x}Pt_x$	23
		surface termination				
B-site composition	reversibility	B-site cation attraction	d, m	La	$Fe_{1-x}Pt_x$	24
					$Fe_{1-x}Rh_x$	
A-site composition	reversibility	B-site surface segregation	d	La	$Fe_{1-x}Pt_x$	25
B-site composition		O vacancy formation		Ca	$Fe_{1-x}Rh_x$	
					$Fe_{1-x}Pd_x$	
B-site composition	reversibility	B-site surface segregation	d	La	$Fe_{1-x}Pt_x$	26
		O vacancy formation			$Fe_{1-x}Rh_x$	
					$Fe_{1-x}Pd_x$	
substrate/film lattice mismatch	density	strain	e, d, m	$La_{0.6}Sr_{0.4}$	Fe	27
reduction temperature		surface defect concentration				
manganates						
B-site composition	exsolveability	B-site cation segregation	e, d	PrBa	$Mn_{1.7}Co_{0.3}$	28
		O vacancy formation			$Mn_{1.7}Ni_{0.3}$	
					$Mn_{1.7}Mn_{0.3}$	

B

Table 1. continued

design parameters	tuned nanoparticle properties	underlying perovskite properties	study type[b]	ABO$_{3-\delta}$ A	B (exsolved)	refs
reduction temperature reduction pO$_2$	exsolveability	crystal reconstruction B vacancy formation energy	e, d	PrBa	Mn$_{1.7}$**Fe$_{0.3}$** Mn$_{0.9}$**Co$_{0.1}$**	29
other						
-	exsolveability	B-site surface segregation	e, d	Sr$_2$	**Fe$_{1.3}$**Mo$_{0.5}$**Ni$_{0.2}$**	30
B-site composition reduction temperature reduction time	size	phase stability	e	La	Al$_{1-x}$**Ni$_x$**	31
reduction time reduction pO$_2$	size	B-site surface segregation concentration of exsolveable ions strain cation diffusion	e, d, m	La$_{0.4}$Sr$_{0.4}$	Sc$_{0.9}$**Ni$_{0.1}$**	32

[a]Studies are grouped by the host (nonexsolved) B-site cation of materials studied. Titanates are most frequently studied, followed by ferrites and manganates. The underlying perovskite properties responsible for the impact of certain design parameters on nanoparticle properties remain unclear. Expanding this table should help resolve these uncertainties and make exsolution cermets more tunable and attractive. [b]e, d, and m indicates that a study employed experiments, DFT calculations, and other modelling respectively.

strategies to design exsolution cermets limits their commercial use.

When engineering exsolution cermets, design parameters (e.g., perovskite composition, exsolution conditions) determine perovskite properties (e.g., surface morphology, phase stability), which in turn determine the final properties of the exsolved NPs (e.g., size, surface density). Within this context, it is key to both (1) correlate design parameters and NP properties and (2) identify the perovskite properties underlying these correlations. Focus on these two aspects together can enable rational design and identification of novel design parameters. In Table 1, we summarize selected works within this framework, grouped by the host (nonexsolving) B-site cation of the studied perovskite compositions. Studies generally first identify correlations between design parameters and NP properties, then turn to characterization, empirical modeling (e.g., models for NP growth kinetics), or density functional theory calculations (DFT) to identify underlying perovskite properties. 52% of the works surveyed study titanate perovskites, while 26 and 9% study ferrites and manganates, respectively. The reduction conditions are the most frequently investigated design parameters, with 43% of surveyed works systematically modifying reduction atmosphere, temperature, and/or time to access different NP properties. It is generally understood that more severe reduction over longer times produces larger, less-numerous NPs.[16−19,31,32] Strain has also emerged as an important characteristic and, when carrying out exsolution on perovskite thin films, a viable design parameter. Several studies have explained exsolved metal NP dimensions with strain-based models,[3,32] while both compressive[14] and tensile[27,33] strains have been observed to promote exsolution of more numerous, smaller NPs. Perovskites' ability to form a wide variety of solid solutions can allow tuning of NP properties through modification of the A-site and B-site chemical composition. The most successful strategy has been the introduction of A-site vacancies, which enhance exsolution thermodynamics and kinetics in titanates[12,13,20,34] and chromites.[6,35] Still, it is difficult to establish universal design principles that allow prediction of NP properties for arbitrary compositions. Considering the wide applicability of cermet and ceramic materials in current and future technologies, such principles are essential if we wish to design exsolution catalysts

that balance catalytic activity with other relevant material properties, such as mechanical strength, ionic conductivity, and cost.

Perovskite chemical composition is particularly critical in determining exsolution properties and overall material performance. As an example, let us consider the design of an exsolution solid oxide fuel cell anode. Here, Ni-doped SrTiO$_3$ solid solutions (STN) are a reasonable material choice. STN is a relatively well-characterized exsolution material with vigorous Ni exsolution and good performance as a steam electrolysis electrode[12] and steam methane reforming catalyst.[13] Aside from driving exsolution, reduction of STN also generates excess oxygen vacancies compensated by Ti^{3+}, resulting in a material with suitably high *n*-type conductivity. To improve conductivity further, a material engineer may be tempted to increase the concentration of Ti^{3+} by substituting La^{3+} onto STN's Sr site.[36−38] However, this strategy would backfire, as La substitutional defects suppress Ni exsolution in this system.[20] Lower NP surface densities would ultimately reduce the length of the triple phase boundaries—the interface between gas, metal, and oxide—and lower the performance in the final fuel cell.[39] This example highlights the trade-offs that can arise when designing exsolution materials. Such trade-offs must be identified, understood, and overcome to apply exsolution cermets commercially.

The STN system mentioned above is relatively well studied, with several works investigating the influence of both La substitutional defects and Sr vacancies on the A site.[12,13,20] However, questions remain. First, there is some debate on the combined effect of Sr vacancies and La substitutional defects on NP density. Some argue that the two defects interact synergistically to increase NP density,[12,13] while others argue that any amount of La substitution reduces NP density.[20] Second, and critically, the phenomena through which the two defects modify NP density are unclear. Post-exsolution characterization via electron microscopy and X-ray spectroscopy point to several possibilities including surface terracing, Sr cation surface segregation, Ni transport, phase stability,[12] surface roughness,[13] surface orientation,[13,15] strain,[14] and Ni cation surface segregation, the last of which is supported by density functional theory (DFT) calculations.[20,32]

Regardless of the phenomena controlling NP properties, tuning exsolution materials would be facilitated by the development of *descriptors* for exsolution, i.e., readily obtainable material parameters which correlate to NP properties. A few attractively simple descriptors have been proposed to predict NP density in STN given the A-site composition, namely A-site cation nonstoichiometry and O nonstoichiometry (as determined by charge balance). It was found that moderate negative A-site cation nonstoichiometry and an O nonstoichiometry close to zero promote the formation of numerous, evenly dispersed NPs.[12] Descriptors based on DFT models have also been introduced. In particular, the surface segregation energetics of exsolveable cations have shown considerable promise,[20,28,33] including a survey by Gao et al. correlating NP density of $SrTi_{0.9}Ni_{0.1}O_{3-\delta}$, $Sr_{0.8}Ti_{0.9}Ni_{0.1}O_{3-\delta}$, $Sr_{0.9}La_{0.1}Ti_{0.9}Ni_{0.1}O_{3-\delta}$ and $Sr_{0.72}La_{0.08}Ti_{0.9}Ni_{0.1}O_{3-\delta}$ with DFT calculations.[20] Descriptors based on DFT models require some effort to calculate but can open the door to predictive design and high-throughput computational screening. If carefully validated, calculations can also provide atomic-level insight into the exsolution mechanism.

In this work, we tuned exsolution in Ni-doped $SrTiO_3$ (STN) through modification of chemical composition and then qualitatively and quantitatively explained our experimental findings with DFT. We investigated the influence of Sr deficiency and La doping on the Sr site—previously investigated by Gao et al.[20]—as well as Ca and Ba doping, again on the Sr site—which to our knowledge have not been systematically analyzed experimentally or computationally. Using DFT calculations, we built a quantitative model that reproduced our experimental trends. Our model suggests that the ease of Ni surface segregation and O loss from Ni-rich perovskite surfaces determines the final nanoparticle density. We also found the DFT-derived driving force of Ni surface segregation to be a promising descriptor for the computational design of exsolution perovskites, though the relationship with nanoparticle density we uncovered diverges from that presented so far in the literature. Covering 11 compositions in total, this study is the largest joint experimental and DFT exsolution study to date. Our results and conclusions should be helpful in identifying and surmounting the obstacles standing in the way of rational design of exsolution materials and help bring these materials closer to commercial feasibility.

2. RESULTS AND DISCUSSION

2.1. Exsolution and Characterization of A-Site Defective Ni-Doped $SrTiO_3$.

To probe the influence of individual A-site defects on metal nanoparticle (NP) properties after exsolution, we experimentally investigated the exsolution of $SrTi_{0.94}Ni_{0.06}O_{3-\delta}$ (STN) solid solutions containing up to 10 mol % defects on the perovskite's structural A-site. After consideration of defect charge and valence, we designed five compositions with the general form $A(Ti_{0.94}Ni_{0.06})O_{3-\delta}$ with A = $Sr_{1.0}$, $Sr_{0.9}$, $Sr_{0.9}Ca_{0.1}$, $Sr_{0.9}La_{0.1}$, and $Sr_{0.9}Ba_{0.1}$ (Figure 2a). Expressed in Kröger−Vink notation, the later four of these compositions contain 10 mol % V''_{Sr}, Ca^x_{Sr}, $La^\bullet_{Sr}$, and Ba^x_{Sr}. The ions Ca^{2+}, Sr^{2+}, and Ba^{2+} are isovalent with Shannon[40] radii of 114, 132, and 149 pm, so through analysis of $Sr_{0.9}Ca_{0.1}Ti_{0.94}Ni_{0.06}O_{3-\delta}$, $SrTi_{0.94}Ni_{0.06}O_{3-\delta}$, and $Sr_{0.9}Ba_{0.1}Ti_{0.94}Ni_{0.06}O_{3-\delta}$, we isolated the influence of dopant size on the exsolved metal NP properties. La^{3+} and Ca^{2+} have different valences but similar Shannon[40] ionic radii (117 and
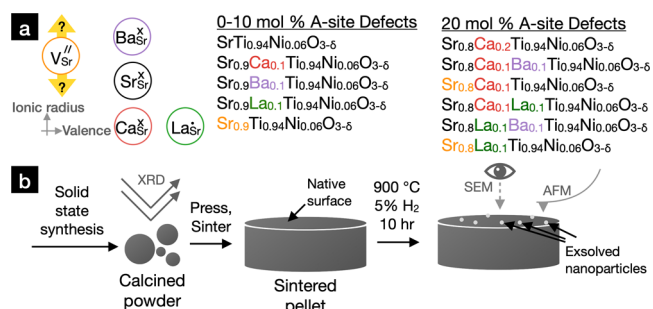
Figure 2. (a) A-site defects, arranged by ionic radii and defect charge, alongside the compositions considered in this work. Sr vacancies do not have a well-defined ionic radius. (b) Synthesis, processing, and characterization performed to measure metal nanoparticle density and radius after exsolution.

114 pm), so by comparing $Sr_{0.9}La_{0.1}Ti_{0.94}Ni_{0.06}O_{3-\delta}$ and $Sr_{0.9}Ca_{0.1}Ti_{0.94}Ni_{0.06}O_{3-\delta}$, we isolated the influence of dopant charge. We analyzed $Sr_{0.9}Ti_{0.94}Ni_{0.06}O_{3-\delta}$ as well to evaluate the impact of A-site deficiency on NP properties.

We manufactured and analyzed exsolved ceramic pellets for all five compositions (Figure 2b). We prepared powders via solid-state synthesis by calcination of ball-milled precursors at 1400 °C for 10 h under air. We performed X-ray diffraction (XRD) to verify the formation of the perovskite phase. We pressed green bodies with a uniaxial press at 2000 bar then sintered the pellets at 1500 °C for 5 h under air. To drive exsolution of Ni NPs, we reduced each pellet at 900 °C under a continuous flow of 5% H_2 balanced with Ar for 10 h. After exsolution, we analyzed the microstructure and measured NP density and radii using scanning electron microscopy (SEM). In addition, we measured NP radii and heights using atomic force microscopy (AFM).

XRD patterns for all compositions are shown in Figure 3a and are analyzed in detail in Section 1 in the Supporting Information. The patterns corresponded closely to those expected from a cubic perovskite (space group *Pm*-3*m*, No. 221) with minute impurity peaks, indicating the formation of the target compositions. Rietveld refinements indicated that the patterns were consistent with a cubic *Pm*-3*m* space group, though slight tilting of the B-site octahedra cannot be ruled out. These refinements yielded a pseudocubic lattice parameter of a = 3.902 Å for $SrTi_{0.94}Ni_{0.06}O_{3-\delta}$. For $Sr_{0.9}Ca_{0.1}Ti_{0.94}Ni_{0.06}O_{3-\delta}$, the pseudocubic lattice parameter decreased to 3.898 Å, a consequence of Ca^{2+}'s smaller ionic radii. For $Sr_{0.9}Ba_{0.1}Ti_{0.94}Ni_{0.06}O_{3-\delta}$, the pseudocubic lattice parameter increased to 3.912 Å, reflecting Ba's larger size. $Sr_{0.9}La_{0.1}Ti_{0.94}Ni_{0.06}O_{3-\delta}$ had a pseudocubic lattice parameter of 3.906 Å. Although La is smaller than Sr, La substitution is known to increase $SrTiO_3$'s lattice parameters due to its higher valence (though the precise electronic cause remains an active area of research).[41] $Sr_{0.9}Ti_{0.94}Ni_{0.06}O_{3-\delta}$ had a slightly expanded pseudocubic lattice parameter of 3.905 Å, in agreement with previous measurements of A-site deficient $SrTiO_3$.[42]

Representative SEM images for all compositions after exsolution are shown in Figure 3b. After exsolution, rounded NPs were visible for all compositions. All perovskite phase constituents of the cermets exhibit faceted grains with some terracing visible. On average, $SrTi_{0.94}Ni_{0.06}O_{3-\delta}$ had 0.9 ± 0.4 μm diameter grains. Modification of this nominal composition with 10 mol % V''_{Sr}, La^x_{Sr}, Ca^x_{Sr}, and Ba^x_{Sr} resulted in average grain diameters of 1.5 ± 0.8, 1.2 ± 0.6, 1.3 ± 0.6, and 0.9 ± 0.6 μm
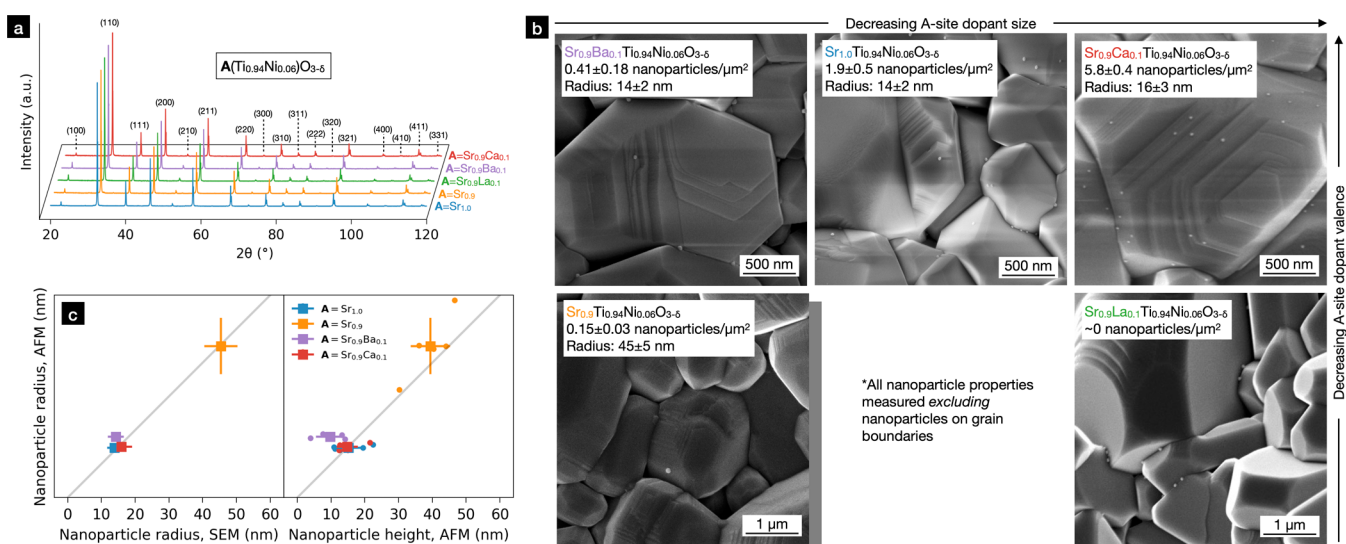
Figure 3. Characterization results for $A(Ti_{0.94}Ni_{0.06})O_{3-\delta}$ materials where A = $Sr_{1.0}$, $Sr_{0.9}$, $Sr_{0.9}Ca_{0.1}$, $Sr_{0.9}La_{0.1}$, and $Sr_{0.9}Ba_{0.1}$. (a) X-ray diffraction patterns of as-calcined powders. Bragg peaks corresponded well to a cubic perovskite structure, indicating successful synthesis. (b) Representative SEM images of pellet surfaces after 10 h treatment at 900 °C under 5% H_2 in Ar. All materials exsolved spherical nanoparticles. Doping with smaller, lower valence dopants resulted in the highest nanoparticle surface densities. (c) Particle radii and heights measured by AFM and SEM. Nanoparticle radii measured by SEM and AFM were in excellent agreement. Nanoparticle radius and height were roughly equal, consistent with spherical nanoparticles roughly halfway immersed into the perovskite backbone.

in the ceramics, respectively. Since all materials were processed and sintered identically, we can surmise that the changes in A-site chemical composition caused the variations in average grain diameters (see Section 2 of the Supporting Information). For $Sr_{0.9}Ca_{0.1}Ti_{0.94}Ni_{0.06}O_{3-\delta}$ and $Sr_{0.9}Ti_{0.94}Ni_{0.06}O_{3-\delta}$, NPs exsolved primarily on individual grains with some NPs exsolving at the grain boundaries. For $SrTi_{0.94}Ni_{0.06}O_{3-\delta}$ and $Sr_{0.9}Ba_{0.1}Ti_{0.94}Ni_{0.06}O_{3-\delta}$, roughly half of the visible NPs exsolved on the individual grains with the remainder appeared at the grain boundaries. For $Sr_{0.9}La_{0.1}Ti_{0.94}Ni_{0.06}O_{3-\delta}$, all observed NPs were located at the grain boundaries.

For each exsolved pellet, we evaluated NP density from SEM images of three randomly chosen regions of the pellet surfaces (Table S1). Image areas were large—ranging between 40 and 90 μm^{-2}—to ensure robust measurements, since exsolution on our samples was inhomogeneous on small length scales. By averaging NP properties measured for each of the three regions, we were able to obtain representative NP densities and radii for each composition. Nucleation behavior is expected to be significantly different on grain boundaries than on the faces of individual grains. Therefore, NPs located at grain boundaries were ignored in this analysis.

$Sr_{0.9}Ca_{0.1}Ti_{0.94}Ni_{0.06}O_{3-\delta}$ had the highest NP density of 5.8±0.4 μm^{-2}, followed by $SrTi_{0.94}Ni_{0.06}O_{3-\delta}$ (1.9±0.5 μm^{-2}), $Sr_{0.9}Ba_{0.1}Ti_{0.94}Ni_{0.06}O_{3-\delta}$, (0.41±0.18 μm^{-2}), and $Sr_{0.9}Ti_{0.94}Ni_{0.06}O_{3-\delta}$ (0.15±0.03 μm^{-2}). $Sr_{0.9}La_{0.1}Ti_{0.94}Ni_{0.06}O_{3-\delta}$ had the lowest NP density, with no NPs visible (apart from those on the grain boundaries). Overall, these materials exsolved rather poorly; this is not unusual for bulk materials and is likely due to a high degree of A-site segregation, which is known to inhibit exsolution.[12,13] $Sr_{0.9}Ti_{0.94}Ni_{0.06}O_{3-\delta}$ had the largest average NP radii: 45±5 nm. $SrTi_{0.94}Ni_{0.06}O_{3-\delta}$, $Sr_{0.9}Ba_{0.1}Ti_{0.94}Ni_{0.06}O_{3-\delta}$, and $Sr_{0.9}Ca_{0.1}Ti_{0.94}Ni_{0.06}O_{3-\delta}$ had similar NP radii: 14 ± 2, 14 ± 2, and 16 ± 3 nm. These values were in good agreement with AFM measurements (Figure 3c). Furthermore, NP radius and protrusion from the

surface were roughly equal, consistent with spherical NPs halfway immersed into the perovskite backbone (Figure 3c).

Through the choice of Ca and Ba dopants at a fixed concentration on the Sr site of $SrTi_{0.94}Ni_{0.06}O_{3-\delta}$, we could probe the impact of ionic radii of A-site dopants on NP density and size. The Shannon[40] ionic radii of Ca^{2+} and Ba^{2+} are 114 and 149 pm, respectively, 86 and 113% that of Sr^{2+} (132 pm). $SrTi_{0.94}Ni_{0.06}O_{3-\delta}$ had an NP density of 1.9±0.5 μm^{-2} compared to 5.8±0.4 μm^{-2} for $Sr_{0.9}Ca_{0.1}Ti_{0.94}Ni_{0.06}O_{3-\delta}$, a significant increase. Meanwhile, $Sr_{0.9}Ba_{0.1}Ti_{0.94}Ni_{0.06}O_{3-\delta}$ had an NP density of 0.41 ± 0.18 μm^{-2}, significantly less than $SrTi_{0.94}Ni_{0.06}O_{3-\delta}$. Therefore, we conclude that the substitution of smaller cations increases NP density while the substitution of larger cations has the opposite effect. Interestingly, the substitution of 10 mol % Ba or Ca on the Sr site of $SrTi_{0.94}Ni_{0.06}O_{3-\delta}$ did not significantly change NP size.

Through the choice of Ca and La dopants at a fixed concentration on the Sr site of $SrTi_{0.94}Ni_{0.06}O_{3-\delta}$, we gauged the impact of A-site dopant valence on NP properties. La and Ca have similar ionic sizes (Shannon[40] radii of 117 and 114 pm, respectively) but have different formal valences (3+ and 2+). After reduction, $Sr_{0.9}La_{0.1}Ti_{0.94}Ni_{0.06}O_{3-\delta}$ exhibited no NPs on grain surfaces while $Sr_{0.9}Ca_{0.1}Ti_{0.94}Ni_{0.06}O_{3-\delta}$ exsolved 5.8 ± 0.4 NPs per μm^{-2}. This indicates that the inclusion of A-site defects with higher valence dramatically hinders exsolution. Assuming Ni is in the 2+ oxidation state, charge balance dictates the compositions $Sr_{0.9}La_{0.1}Ti_{0.94}Ni_{0.06}O_{2.99}$ (δ = 0.01) and $Sr_{0.9}Ca_{0.1}Ti_{0.94}Ni_{0.06}O_{2.94}$ (δ = 0.06). Therefore, our result is consistent with a previous report[12] in which greater oxygen deficiency promoted exsolution by decreasing Ni's solubility in reduced STN.

By comparing $SrTi_{0.94}Ni_{0.06}O_{3-\delta}$ and $Sr_{0.9}Ti_{0.94}Ni_{0.06}O_{3-\delta}$, we assessed the impact of 10 mol % Sr deficiency on NP properties. $Sr_{0.9}Ti_{0.94}Ni_{0.06}O_{3-\delta}$ had an NP density of 0.15 ± 0.03 μm^{-2}, an order of magnitude lower than that of $SrTi_{0.94}Ni_{0.06}O_{3-\delta}$ (1.9 ± 0.5 μm^{-2}). This was unexpected, as it is well established that Sr deficiency promotes exsolu-

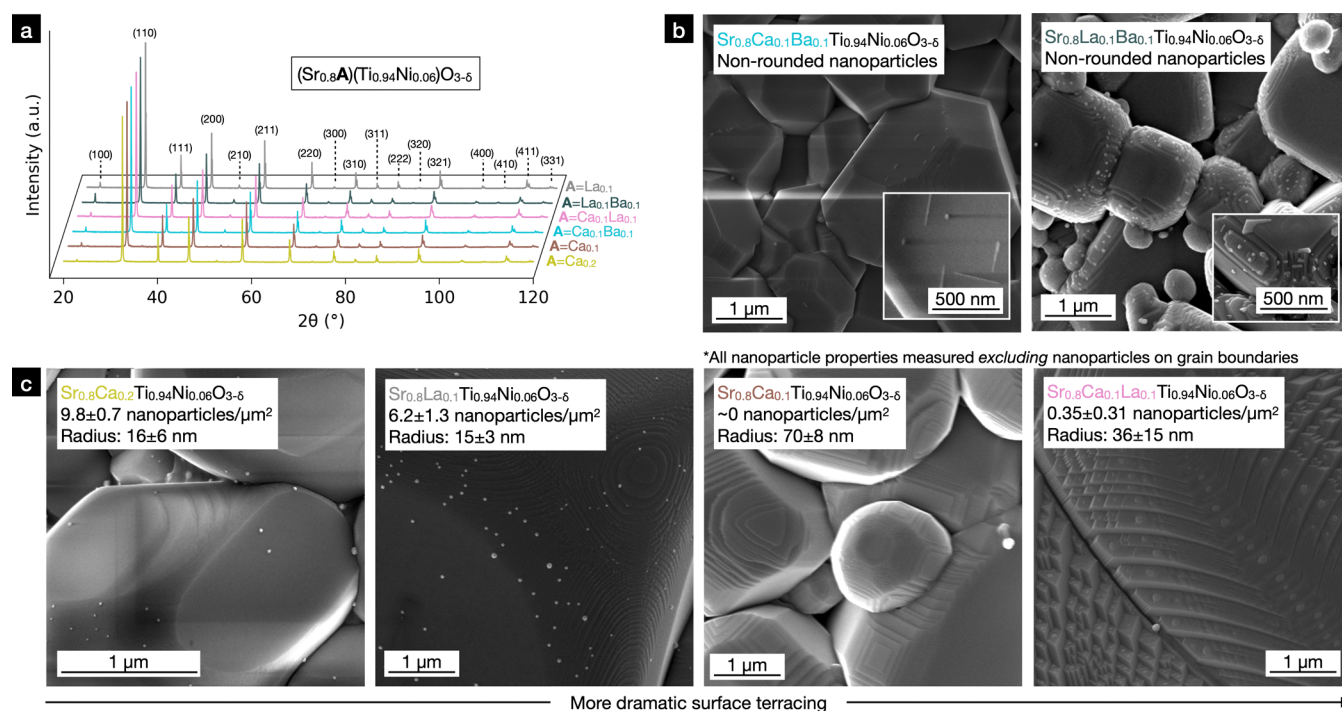**Figure 4.** Characterization results for $(Sr_{0.8}A)(Ti_{0.94}Ni_{0.06})O_{3-\delta}$ materials where A = $Ca_{0.1}La_{0.1}$, $Ca_{0.1}$, $Ca_{0.2}$, $Ca_{0.1}Ba_{0.1}$, $La_{0.1}$, and $La_{0.1}Ba_{0.1}$. (a) X-ray diffraction patterns of as-calcined powders. Patterns corresponded well to a cubic perovskite structure, except in the case of $Sr_{0.8}Ca_{0.1}La_{0.1}Ti_{0.94}Ni_{0.06}O_{3-\delta}$ which showed signs of substantial tilting of B-site octahedra. (b) Representative SEM images of $Sr_{0.8}Ca_{0.1}Ba_{0.1}Ti_{0.94}Ni_{0.06}O_{3-\delta}$ and $Sr_{0.8}La_{0.1}Ba_{0.1}Ti_{0.94}Ni_{0.06}O_{3-\delta}$ after exsolution, both of which exhibited unusual nanoparticle morphologies. (c) Representative SEM images of samples exhibiting typical nanoparticle morphologies. These materials had highly variable surface morphologies and grain sizes.

tion.[6,12,13,20,34,35] NPs exsolved from $Sr_{0.9}Ti_{0.94}Ni_{0.06}O_{3-\delta}$ were larger than those of the other samples, suggesting that exsolution may indeed have been promoted but NP growth was favored over NP nucleation. It was previously found that Sr deficiency must be tuned to achieve an optimal tradeoff between nucleation and growth.[12] Therefore, our material is likely in the regime where growth is highly favored.

Through careful choice of composition and successful synthesis and characterization, we demonstrated that smaller, lower valence A-site dopants lead to higher NP densities in $SrTi_{0.94}Ni_{0.06}O_{3-\delta}$ without changing the NP size. The introduction of 10 mol % Sr vacancies or La to $SrTi_{0.94}Ni_{0.06}O_{3-\delta}$ led to fewer NPs. Given these results, we focused next on compositions containing our smallest dopants: La and Ca. Specifically, we wished to determine how the introduction of A-site vacancies or other A-site dopants alongside Ca or La dopants influenced NP properties. Samples with compositions of the form $(Sr_{0.8}A)(Ti_{0.94}Ni_{0.06})O_{3-\delta}$, where A = $Ca_{0.1}La_{0.1}$, $Ca_{0.1}$, $Ca_{0.2}$, $Ca_{0.1}Ba_{0.1}$, $La_{0.1}$, and $La_{0.1}Ba_{0.1}$ were prepared, exsolved, and characterized in an identical manner to those made previously. XRD patterns for the as-synthesized powders are shown in Figure 4a. Almost all patterns indicated a cubic (or nearly cubic) perovskite structure with some containing weak impurity peaks. The pattern for $Sr_{0.8}Ca_{0.1}La_{0.1}Ti_{0.94}Ni_{0.06}O_{3-\delta}$ exhibited clear signs of octahedral tilting, consistent with several tilt systems theorized by Glazer.[43] Additional analysis can be found in Section 1 of the Supporting Information. Representative SEM images of the materials after exsolution are shown in Figure 4b,c.

Rectangular exsolutions were visible on $Sr_{0.8}Ca_{0.1}Ba_{0.1}Ti_{0.94}Ni_{0.06}O_{3-\delta}$, while on $Sr_{0.8}La_{0.1}Ba_{0.1}Ti_{0.94}Ni_{0.06}O_{3-\delta}$ highly angular, plate-like NPs

nucleated preferentially around the terrace-like motifs (Figure 4b). Nonspherical metal exsolution NPs have been previously observed, for example after reduction under moderate reducing conditions.[3] However, given the extremely reducing conditions used in our experiments and the low reducibility of the non-Ni cations present in these perovskites, we hypothesize that these unusual exsolutions are not Ni but instead an oxide of one or more of the cations. Among the four compositions with typical, rounded NP morphologies (Figure 4c), the surface morphology of the perovskite was highly variable. The two compositions containing only isovalent dopants on the A site—$Sr_{0.8}Ca_{0.2}Ti_{0.94}Ni_{0.06}O_{3-\delta}$ and $Sr_{0.8}Ca_{0.1}Ba_{0.1}Ti_{0.94}Ni_{0.06}O_{3-\delta}$—had relatively flat facets, like the compositions examined previously. All other compositions developed terrace-like surface motifs, the most dramatic example being $Sr_{0.8}Ca_{0.1}La_{0.1}Ti_{0.94}Ni_{0.06}O_{3-\delta}$. Substantial variation in microstructure was also present, with grain diameters ranging from 1.0 ± 0.6 μm for $Sr_{0.8}La_{0.1}Ba_{0.1}Ti_{0.94}Ni_{0.06}O_{3-\delta}$ to 12 ± 5 μm for $Sr_{0.8}Ca_{0.1}La_{0.1}Ti_{0.94}Ni_{0.06}O_{3-\delta}$.

Substitution of Sr with Ca again led to significantly higher NP density, with $Sr_{0.8}Ca_{0.2}Ti_{0.94}Ni_{0.06}O_{3-\delta}$ having an NP density of 9.8 ± 0.7 μm^{-2} ($Sr_{0.9}Ca_{0.1}Ti_{0.94}Ni_{0.06}O_{3-\delta}$'s NP density was 5.8 ± 0.5 μm^{-2}). The introduction of additional Ca did not significantly change the NP size. This fits with our previous observations that the sole introduction of isovalent cations on the Sr site modifies NP density without significantly changing NP size. Introduction of Sr vacancies or La onto the A site alongside Ca sharply suppressed NP density, with $Sr_{0.8}Ca_{0.1}La_{0.1}Ti_{0.94}Ni_{0.06}O_{3-\delta}$ and $Sr_{0.8}Ca_{0.1}Ti_{0.94}Ni_{0.06}O_{3-\delta}$ yielding 0.35 ± 0.31 and essentially zero NPs per μm^{-2}, respectively. Accompanying this was an increase in the NP size, consistent with our previous observations. Interestingly, a
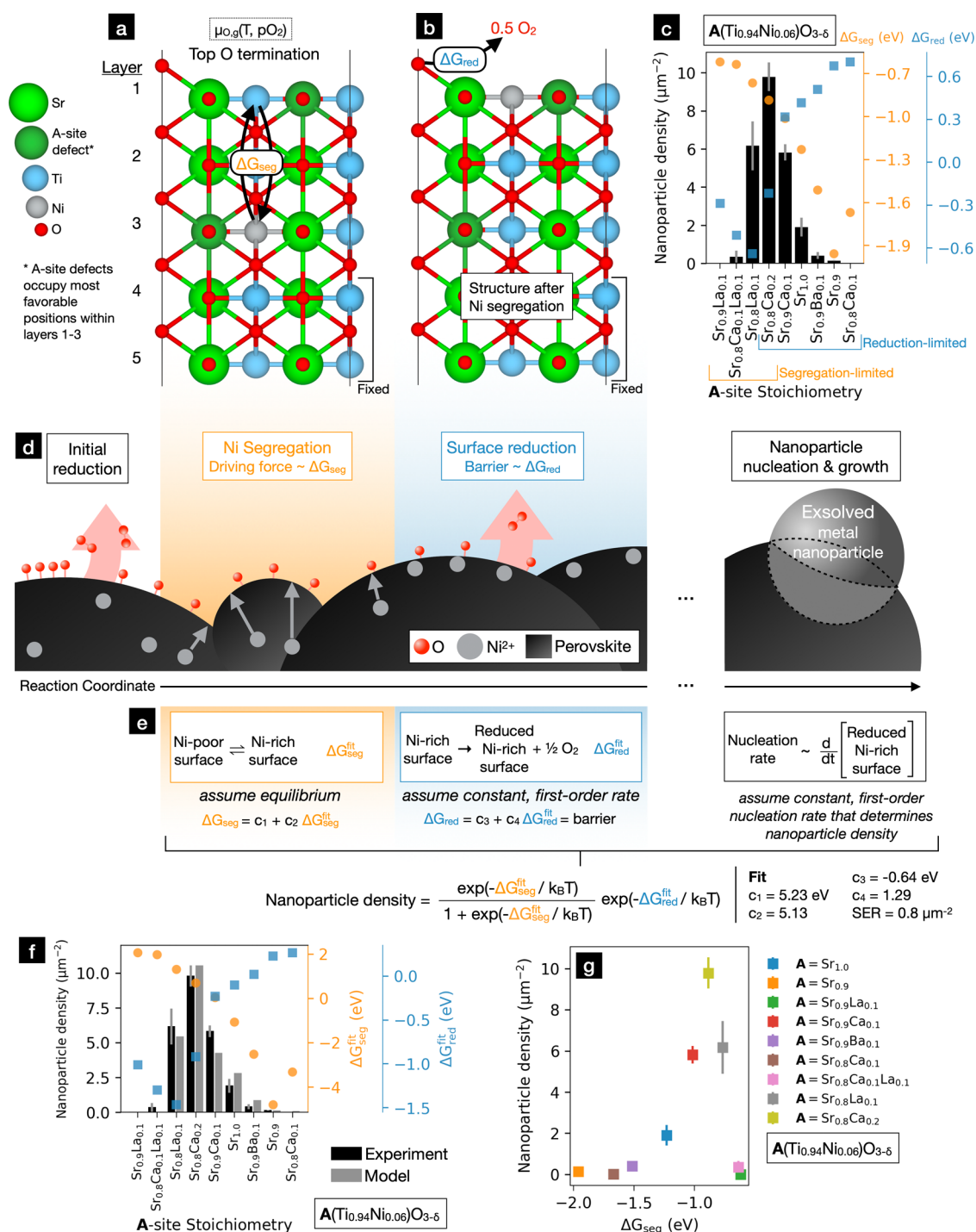
Figure 5. (a) (110) Oriented slab model used to calculate the segregation energy ΔG_{seg} defined as the energy change upon swapping Ni and Ti between the first and third layers. The most stable surface O termination under exsolution conditions (900 °C, $pO_2 = 10^{-25}$ atm) was used. (b) Definition of reduction energy ΔG_{red}, the energy change upon removal of a single surface O following Ni segregation. (c) Post-exsolution nanoparticle density for all compositions plotted alongside calculated ΔG_{seg} and ΔG_{red}. Two regimes are apparent, one with more positive ΔG_{seg} (segregation-limited) and another where the opposite is the case (reduction-limited). There is a roughly inverse relationship between ΔG_{seg} and ΔG_{red}. (d) Our proposed partial exsolution mechanism. NP density is controlled by two consecutive steps in the mechanism: Ni segregation and surface reduction. (e) Quantitative model for prediction of nanoparticle density based on our proposed mechanism and DFT calculations. (f) Experimentally measured nanoparticle density vs nanoparticle density predicted by our fitted model. The model performed well. (g) Experimentally measured nanoparticle density vs calculated ΔG_{seg}. Nanoparticle density has a volcano-like dependence on ΔG_{seg}, with moderate values around 0.9 eV yielding the highest nanoparticle densities.

combination of La and Sr vacancies led to NP densities and sizes comparable to the compositions with only isovalent doping. We attribute these effects to the charge compensation

of La dopants (1+ charge) by Sr vacancies (2- charge). This synergistic effect between the two defects agrees with earlier work by Neagu _et al._[13] and contradicts work by Gao et al.,[20]

who found that La doping decreased NP density even in Sr-deficient compositions. Considering La and Ca's similar ionic radii, we would therefore expect that La dopants in the presence of compensated Sr vacancies would produce a similar effect as Ca doping alone. Indeed, $Sr_{0.9}Ca_{0.1}Ti_{0.94}Ni_{0.06}O_{3-\delta}$ and $Sr_{0.8}La_{0.1}Ti_{0.94}Ni_{0.06}O_{3-\delta}$ had similar exsolution properties.

So far, we have discussed trends in NP radius and density in a primarily qualitative manner disconnected from the underlying exsolution mechanism and perovskite properties. Seeking a universal descriptor with a clear link to material characteristics that would allow prediction of NP properties for arbitrary compositions, we turned to DFT calculations.

2.2. DFT Calculations and Derivation of a Predictive Model.

Gao et al.[20] previously showed that compositions with more favorable Ni segregation energies—calculated by swapping Ni and Ti between the surface and bulk sites of a slab model—had higher NP densities. Using Gao et al.'s work as a starting point, we used DFT to calculate Ni segregation energies, denoted as ΔG_{seg}, for slab models with the general composition $A(Ti_{0.9}Ni_{0.1})O_{3-\delta}$ where $A = Sr_{1.0}$, $Sr_{0.9}$, $Sr_{0.9}Ca_{0.1}$, $Sr_{0.9}La_{0.1}$, $Sr_{0.9}Ba_{0.1}$, $Sr_{0.8}Ca_{0.1}La_{0.1}$, $Sr_{0.8}Ca_{0.1}$, $Sr_{0.8}Ca_{0.2}$, and $Sr_{0.8}La_{0.1}$. We used a (110) oriented (defined for the cubic perovskite unit cell) slab model as shown in Figure 5a. NP properties are strongly dependent on perovskite surface orientation,[15] but we focused solely on the (110) termination—which exsolves particularly vigorously[13]—to limit computational expense. We fixed the bottom two layers of all slabs to their bulk positions and considered the middle-most and top layers as simulating the perovskite bulk and surface, respectively. The stoichiometries of our slab models had A-site defect concentrations nominally identical to the compositions that experimentally exhibited exsolution of rounded NPs. Due to their small size, our structures were limited to 10 mol % Ni substituted on the B site (compared to the 6 mol % substitution in the experimental compositions). Since we wanted to examine trends, we judged this difference acceptable. Up to two A-site defects were placed within the top three layers of our slab models. Each defect was moved vertically between the top three layers and placed in its most favorable position.

We calculated ΔG_{seg} with a strong emphasis on approaching the "thermodynamic limit" of Ni segregation. We used the most favorable locations of the A-site defects for our pre- and post-segregation structures. Since O nonstoichiometry under reducing conditions is the key driver of exsolution, we expended considerable effort determining the quantity and arrangement of oxygens in the slab model based on *ab initio* thermodynamics.[44,45] In our model, O could be removed from the bulk (to form O vacancies) or from the surface (to alter the top O termination). We considered including O vacancies in the third layer of the slab, but we did not pursue this further since accommodating O nonstoichiometry on the top surface (though modification of the surface O termination) was thermodynamically favored (Figure S3). Although we always used a SrTiO bottom termination, in most cases we utilized $SrTiO_x$ terminations on the top surface where $x > 1.0$, as we found that these oxygen-richer terminations were most favorable under the exsolution conditions (900 °C, $pO_2 = 10^{-25}$ atm) (Figure S3). This preliminary work was important, as the O content on the surface had large effects on the electronic structure of the surface as well as the Ni dopant (Figure S4) and strongly influenced calculated segregation energies (Figures S5 and S6). As a reference, we calculated ΔG_{seg} for all compositions with the surface O termination fixed at SrTiO as done by Gao et al.[20] This produced very different results compared to calculations where surface O termination was determined in a thermodynamically consistent way (Figure S7). Finally, we found that the surface O termination of La-containing compositions required special treatment. Our small slab model lacked the granularity to capture La's influence on the surface O termination, but we developed an interpolation-based approach to estimate ΔG_{seg} for La-containing compositions (Figure S8).

While calculating ΔG_{seg}, we noted that Ni remained oxidized after segregation in all compositions. Therefore, we hypothesized that the removal of additional surface O after Ni segregation is required for the nucleation and growth of metal NPs. We investigated this process via DFT by calculating the free energy required to liberate an additional surface O following Ni segregation, referred to as ΔG_{red} (Figure 5b). In these calculations, A-site defects were again free to occupy their most favorable positions. For La-containing compositions, an interpolation approach analogous to the one used to calculate ΔG_{seg} was applied.

Figure 5c plots the NP density for all compositions alongside calculated ΔG_{seg} and ΔG_{red}. The inclusion of Sr vacancies and A-site dopants in our calculations had roughly opposite effects on ΔG_{seg} and ΔG_{red}. These effects are in part the result of changes in the models' surface O terminations. In our calculations, La^{3+}'s net positive charge stabilized O-richer surfaces; this increased ΔG_{seg}, as the lack of oxygen at the surface is a major driving force of Ni segregation. O-richer surfaces, however, were easier to reduce, and therefore the inclusion of La decreased ΔG_{red}. Introduction of negatively charged Sr vacancies, meanwhile, stabilized O-poorer surfaces. This decreased ΔG_{seg} and increased ΔG_{red} for the same reasons mentioned above.

The surface O content alone, however, was insufficient to explain the results of our calculations as Ca and Ba substitution—which are isovalent with Sr and therefore did not influence the surface O content—also strongly influenced the calculated energetics. These effects arose from the movement of A-site dopants between the layers of our slab models. Since Ca^{2+} and Ba^{2+} ions are smaller and larger than Sr^{2+}, in isolation both Ca and Ba prefer to segregate to the slab surface.[46] The presence of Ni on the B site, however, leads to co-segregation of Ba and de-segregation of Ca during Ni segregation. Co-segregation and de-segregation of Ba and Ca lead to lower and higher values of ΔG_{seg}, respectively. Ca and Ba's segregation behavior also influenced ΔG_{red}. We found that surface reduction reduces the interlayer distance at the slab surface (Figure S12c), enabling Ca segregation upon reduction (lowering ΔG_{red}). Meanwhile, the segregated Ba ion's relatively large size leads to an energy penalty (increasing ΔG_{red}). In summary, the complex interplay between surface O termination and movement of A-site dopants gave rise to the calculated trends in ΔG_{seg} and ΔG_{red}. A detailed analysis of these effects can be found in Section 10 of the Supporting Information.

Under the hypothesis of Gao et al., more favorable Ni cation segregation should lead to a greater number of NPs, since stronger segregation leads to more Ni cations on the surface and therefore more potential nucleation sites.[20] In contrast, we found that a high ΔG_{seg} or ΔG_{red} corresponded to lower NP densities. The inverse relationship between ΔG_{seg} and ΔG_{red} gave rise to two groups of materials. In one group, ΔG_{seg} is

very favorable and the favorability of ΔG_{red} is positively correlated to NP density. In the other group, ΔG_{red} is very favorable while the favorability of ΔG_{seg} is positively correlated to NP density. We propose that these material groups occupy "reduction-limited" and "segregation-limited" regimes, respectively. $Sr_{0.8}Ca_{0.2}Ti_{0.9}Ni_{0.1}O_{3-\delta}$ could potentially be in either regime (or could lie in a transition regime). In the reduction-limited regime, extremely favorable Ni surface segregation suggests a high amount of Ni cations on the surface during exsolution. However, larger values of ΔG_{red} within this regime indicate that the Ni-enriched surface is relatively hard to reduce. We conclude that the ease of surface reduction controls final NP densities within this regime. In the reduction-limited regime on the other hand, the opposite is the case; ΔG_{red} is quite favorable, and NP density is instead controlled by the ease of Ni surface segregation.

From the correspondence between our DFT and experimental findings, we propose a partial exsolution mechanism as summarized in Figure 5d. Following initial O loss from the perovskite bulk and surfaces upon exposure to a reducing atmosphere, Ni segregates to the surface. Further reduction of the Ni-enriched surfaces then enables the nucleation and growth of NPs. In our experiments, the introduction of A-site defects had opposite effects on the driving forces of Ni segregation and surface reduction. It appears that A-site defects primarily modified the overall stability of Ni-enriched perovskite surfaces. Greater surface stabilization generated a more favorable Ni segregation energy while also making Ni-enriched surfaces more resistant to further breakdown.

Based on this proposed mechanism, we connected our DFT-derived energies to our experimental results through a quantitative model described in Figure 5e. Our model considers three consecutive reactions: Ni surface segregation, surface reduction, and NP nucleation. We describe Ni segregation as an equilibrium between Ni-poor and Ni-rich surfaces

$$(\text{Ni-poor surface}) \rightleftharpoons (\text{Ni-rich surface}) \qquad (1)$$
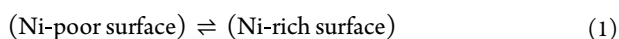
with a driving force expressed as a linear function of ΔG_{seg}

$$G_{seg}^{fit} \equiv c_1 + c_2 \Delta G_{seg} \qquad (2)$$

We envision surface reduction as a reaction between a gaseous H_2 molecule and a dangling surface oxygen in which metal−oxygen bonds are broken and H_2O is formed. The barrier of this reaction should scale with the strength of the metal−oxygen bonds, which is closely related to our DFT-derived thermodynamic driving force ΔG_{red}. Since H_2 concentration was constant in our experiments, we treat surface reduction as a first-order reaction between Ni-rich and reduced Ni-rich surfaces

$$(\text{Ni-rich surface}) \rightarrow (\text{reduced Ni-rich surface}) \qquad (3)$$

with a kinetic barrier ΔG_{red}^{fit} that scales linearly with ΔG_{red}

$$\text{barrier} = \Delta G_{red}^{fit} \equiv c_3 + c_4 \Delta G_{red} \qquad (4)$$

Finally, we describe nucleation as a first-order reaction with a rate proportional to the production rate of reduced Ni-rich surfaces. In other words, we assume that the rate of Ni-rich surface reduction is proportional to the NP nucleation rate.

After working through the algebra associated with the equilibrium and rate expressions (see Section 7 of the Supporting Information), we derived the following model for NP density

$$\text{nanoparticle density} = \frac{e^{\frac{-(c_1+c_2\Delta G_{seg})}{kT}}}{1 + e^{\frac{-(c_1+c_2\Delta G_{seg})}{kT}}} e^{\frac{-(c_3+c_4\Delta G_{red})}{kT}} \qquad (5)$$

This formula contains four fitting parameters—c_1, c_2, c_3, c_4—which relate the model's segregation and reduction energies to our DFT-derived energies. c_3 functions as a prefactor for the entire expression and depends on the units of NP density and the nucleation rate. We performed a least-squared fit of this formula using our DFT and experimental data. The experimentally observed NP densities and the fitted model's predictions vs the model's scaled segregation and reduction energies are presented in Figure 5f. The fitted values are c_1 = 5.23 eV, c_2 = 5.13, c_3 = −0.64 eV, and c_4 = 1.29. c_2 and c_4 were positive, meaning that our fitted segregation and reduction energies were directly proportional to our DFT-calculated energies. The model performed remarkably well, with a standard error of the regression of 0.8 μm^{-2}. In addition, the model helped us rationalize the changes in NP size observed over the course of our experiments (see Section 8 of the Supporting Information). Still, the success of our model is far from irrefutable proof of our proposed exsolution mechanism. Although eq 5 was derived from physical principles and contains energies calculated from first principles, it remains ultimately a semiempirical expression. To better understand our model's physical meaning, further work is needed. More could be learned, for example, by extending the model to understand how other parameters—B-site doping, reduction conditions, etc.—modulate Ni exsolution from $SrTiO_3$.

Examination of ΔG_{seg} alone gives further insights into our model and results. We observed that the interplay between ΔG_{seg} and ΔG_{red} led to a volcano-like correlation between NP surface density and ΔG_{seg} (Figure 5g). This suggests that optimizing NP density under our exsolution conditions can be done by finding a composition with an optimal, moderate ΔG_{seg} located at the "peak" of the volcano. At the same time, our proposed ΔG_{seg} descriptor demonstrates a potential limitation of using A-site doping to increase NP density. Because of the tradeoff between ΔG_{seg} and ΔG_{red}, our work suggests the existence of some optimum ΔG_{seg} and corresponding maximum NP density attainable by tuning A-site composition. Still, our calculations showed that the tradeoff between ΔG_{seg} and ΔG_{red} was not absolute, particularly in systems containing La doping and/or Sr vacancies. Additional DFT calculations on compositions containing charged defects may point to promising compositions that overcome the volcano-like dependence of NP density on ΔG_{seg}.

The success of our quantitative model as well as the volcano-like trend observed between NP density and ΔG_{seg} are remarkable given the wide range of surface morphologies and microstructures we observed experimentally. This encouraging result suggests that our simple model and ΔG_{seg} can be used to engineer the average exsolution properties of materials, which ultimately dictate catalytic performance in real-world applications. In addition, our model and descriptor may be a useful computational tool for evaluating exsolution design parameters beyond changes in bulk A-site composition. Parameters that could be explored include strain and surface-selective doping.

With careful construction of slab models, the influence of local surface structure (terracing, orientation) on NP density could also be studied. Such future work will be helpful in the search for higher performance exsolution catalysts.

3. CONCLUSIONS

The design of perovskite cermet catalysts prepared via exsolution remains challenging due to a shortage of reliable material design guidelines and an incomplete understanding of the exsolution mechanism. We confronted these challenges through experimental and computational study of the influence of A-site defects on the exsolution behavior of perovskites. To begin, we exsolved nanoparticles from 11 perovskite pellets with the general composition $A(Ti_{0.94}Ni_{0.06})O_{3-\delta}$ where A = $Sr_{1.0}$, $Sr_{0.9}$, $Sr_{0.9}Ca_{0.1}$, $Sr_{0.9}La_{0.1}$, $Sr_{0.9}Ba_{0.1}$, $Ca_{0.1}La_{0.1}$, $Sr_{0.8}Ca_{0.1}$, $Sr_{0.8}Ca_{0.2}$, $Sr_{0.8}Ca_{0.1}Ba_{0.1}$, $Sr_{0.8}La_{0.1}$, and $Sr_{0.8}La_{0.1}Ba_{0.1}$. Using scanning electron and atomic force microscopy, we measured how the choice of A changed nanoparticle density and size. We then constructed a DFT-based model that quantitatively fit our measurements. We propose that modification of the perovskite A site inversely tunes the favorability of two key steps in the exsolution mechanism: Ni segregation and reduction of Ni-rich surfaces. Materials with both favorable Ni segregation and favorable reduction of Ni-rich surfaces exhibit the highest particle densities and are therefore expected to have the highest catalytic activity. Our model and insights into the exsolution mechanism can be used to rationally design exsolution cermets and search for new strategies to increase exsolution nanoparticle density. Success in these endeavors would have significant implications for the development of highly active and stable catalysts for modern chemical conversion and energy applications.

4. METHODS

4.1. Material Preparation. Bulk materials with compositions $SrTi_{0.94}Ni_{0.06}O_{3-\delta}$, $Sr_{0.9}Ca_{0.1}Ti_{0.94}Ni_{0.06}O_{3-\delta}$, $Sr_{0.9}Ba_{0.1}Ti_{0.94}Ni_{0.06}O_{3-\delta}$, $Sr_{0.9}La_{0.1}Ti_{0.94}Ni_{0.06}O_{3-\delta}$, $Sr_{0.9}Ti_{0.94}Ni_{0.06}O_{3-\delta}$, $Sr_{0.8}Ca_{0.2}Ti_{0.94}Ni_{0.06}O_{3-\delta}$, $Sr_{0.8}Ca_{0.1}La_{0.1}Ti_{0.94}Ni_{0.06}O_{3-\delta}$, $Sr_{0.8}Ca_{0.1}Ba_{0.1}Ti_{0.94}Ni_{0.06}O_{3-\delta}$, $Sr_{0.8}Ca_{0.1}Ti_{0.94}Ni_{0.06}O_{3-\delta}$, $Sr_{0.8}La_{0.1}Ba_{0.1}Ti_{0.94}Ni_{0.06}O_{3-\delta}$, and $Sr_{0.8}La_{0.1}Ti_{0.94}Ni_{0.06}O_{3-\delta}$ were prepared via a solid-state synthesis route. Stoichiometric quantities of $SrCO_3$ (Alfa Aesar, 99.9%), La_2O_3 (Sigma-Aldrich, 99.9%), $BaCO_3$ (Alfa Aesar, 99.997%), $CaCO_3$ (Sigma-Aldrich, 99%), TiO_2 anatase (Alfa Aesar, 99.6%), and NiO (Alfa Aesar, 99%) powders were mixed by planetary ball milling (PM, Across International, PQ-N04) in pure ethanol with ZrO_2 balls for 1 h at 500 rpm. The resulting slurries were dried for 2 h at 120 °C, ground by a mortar and pestle, and then calcined at 1400 °C for 10 h under air with a 10 °C/min heating rate in Al_2O_3 crucibles. Calcined powders were ground with mortar and pestle. From these calcined powders, 0.15 g pellets were pressed isostatically in a uniaxial press (1000 psi) and sintered at 1500 °C for 5 h under air with a 10 °C/min heating rate on Al_2O_3 plates. Pellets were exsolved by firing at 900 °C for 10 h with a 10 °C/min heating rate under a 200 sccm flow of 5% H_2 (Airgas, ultrahigh purity) balanced with Ar (Airgas, ultrahigh purity). During ramp-up to exsolution temperature, the material was kept under Ar. During cooling after exsolution, a 5% H_2 atmosphere was maintained to inhibit NP reoxidation.

4.2. Material Characterization. The phase composition of as-calcined powders was measured by XRD with a Panalytical X'Pert Pro diffractometer equipped with an X-ray tube using Cu-Kα radiation. An X'Celerator 1D detector, Ni filter, and a fixed divergence slit of 1/2° were used. Rietveld refinements were carried out using the HighScore Plus software. SEM (Carl Zeiss Merlin HR-SEM, Germany) was performed using an in-lens detector and 6 kV accelerating voltage. The nanoparticle number was determined through manual counting with assistance from ImageJ 1.52a[47] and

then divided by image area, resulting in three points per NP density measurement. To further evaluate particle geometry, we conducted atomic force microscopy (AFM) measurements for the five samples with compositions of the form $A(Ti_{0.94}Ni_{0.06})O_{3-\delta}$ with A = $Sr_{1.0}$, $Sr_{0.9}$, $Sr_{0.9}Ca_{0.1}$, $Sr_{0.9}La_{0.1}$, and $Sr_{0.9}Ba_{0.1}$. These measurements were performed with AC-air Topography mode on a Cypher ES instrument (Asylum Research) using a silicon cantilever (AC240TS-R3). For each composition, we measured the individual height and widths of 4−6 nanoparticles using Gwyddion.[48] Additional information is available in Figure S2.

4.3. DFT Calculations. Spin-polarized DFT calculations were performed under the generalized gradient approximation using the Perdew−Burke−Ernzerhof (PBE)[49] functional and a 500 eV plane wave cutoff as implemented in the Vienna Ab initio Simulation Package (VASP).[50−53] To reduce the computational cost, the projector augmented-wave (PAW) method was applied.[53,54] The PAW pseudopotentials included with VASP (v.5.4) were used for all elements. Standard pseudopotentials were used for O and La. For Sr, Ca, and Ba semicore s-states were treated as valence states. For Ti and Ni, semicore p-states were treated as valence states. To better capture long-range forces, the DFT-D3 method with Becke-Johnson damping was applied.[55] To counteract erroneous electron delocalization, $+U$ corrections were applied to Ti and Ni atoms.[56] Values of U_{Ti} = 3 eV, U_{Ni} = 6 eV were utilized. The U value for Ni was similar to the one developed by Wang et al.,[57] while our chosen value for Ti was in the range recommended by ref 58.

Lattice constants for all slabs were determined by a full relaxation of a Ni-doped $SrTiO_{2.875}$ 2 × 2 × 2 supercell ($Sr_7Ni_1Ti_8O_{23}$) with a 2 × 2 × 2 k-point grid. In this bulk calculation, this O nonstoichiometry was found to be favorable under our exsolution conditions. We utilized a 5-layer (110) oriented (with respect to the cubic perovskite unit cell) STN slab model, similar to one utilized by Gao et al.[20] A SrTiO termination was used for the bottom of all slabs, and the atomic coordinates for the bottom two layers were fixed. Surface O termination was selected based on $ab\ initio$ thermodynamics calculations[44,45] with Ni in the third layer of the slab (prior to segregation), as described in the text and Supporting Information. Slabs were separated by 15.5 Å of vacuum to minimize interaction among repeating images. A 2 × 2 × 1 Monkhorst k-point grid[59] was applied (with 1 k-point in the direction perpendicular to the slab surface), except in our calculations on a larger model in which a 2 × 1 × 1 grid was applied. For all calculations, electronic relaxation was performed with a cutoff of 10^{-6} eV, while relaxation of atomic positions was performed until a force threshold of 10^{-2} eV/Å on each relaxing atom was achieved.

ASSOCIATED CONTENT

Ⓢ Supporting Information

The Supporting Information is available free of charge at https://pubs.acs.org/doi/10.1021/jacs.2c12011.

Experimental and computational details, including material characterization, development of atomistic models, and interpretation of DFT calculations (PDF)

AUTHOR INFORMATION

Corresponding Author

Jennifer L. M. Rupp − *Department of Materials Science and Engineering and Department of Electrical Engineering and Computer Science, Massachusetts Institute of Technology, Cambridge, Massachusetts 02139, United States; Department of Chemistry, Technical University of Munich, Garching 85748, Germany;* ⓞ orcid.org/0000-0001-7160-0108; Email: jrupp@tum.de

Authors

Willis O'Leary − *Department of Materials Science and Engineering, Massachusetts Institute of Technology,*

Cambridge, Massachusetts 02139, United States;
 orcid.org/0000-0003-1126-0214

Livia Giordano − *Department of Materials Science, University of Milano-Bicocca, Milan 20125, Italy; Research Laboratory of Electronics, Massachusetts Institute of Technology, Cambridge, Massachusetts 02139, United States;*
 orcid.org/0000-0002-6879-9424

Jieun Park − *Department of Mechanical and Industrial Engineering, University of Massachusetts—Amherst, Amherst, Massachusetts 01002, United States;* orcid.org/0000-0003-2720-9544

Stephen S. Nonnenmann − *Department of Mechanical and Industrial Engineering, University of Massachusetts—Amherst, Amherst, Massachusetts 01002, United States;*
 orcid.org/0000-0002-5369-9279

Yang Shao-Horn − *Department of Materials Science and Engineering, Research Laboratory of Electronics, and Department of Mechanical Engineering, Massachusetts Institute of Technology, Cambridge, Massachusetts 02139, United States;* orcid.org/0000-0001-8714-2121

Complete contact information is available at:
https://pubs.acs.org/10.1021/jacs.2c12011

Notes
The authors declare no competing financial interest.

■ REFERENCES

(1) Anderson, J. A.; García, M. F. *Supported Metals in Catalysis*; Imperial College Press, 2011.

(2) Lavoie, J.-M. Review on Dry Reforming of Methane, a Potentially More Environmentally-Friendly Approach to the Increasing Natural Gas Exploitation. *Front. Chem.* **2014**, *2*, No. 81.

(3) Neagu, D.; Kyriakou, V.; Roiban, I.-L.; Aouine, M.; Tang, C.; Caravaca, A.; Kousi, K.; Schreur-Piet, I.; Metcalfe, I. S.; Vernoux, P.; van de Sanden, M. C. M.; Tsampas, M. N. *In Situ* Observation of Nanoparticle Exsolution from Perovskite Oxides: From Atomic Scale Mechanistic Insight to Nanostructure Tailoring. *ACS Nano* **2019**, *13*, 12996−13005.

(4) Oh, T.-S.; Rahani, E. K.; Neagu, D.; Irvine, J. T. S.; Shenoy, V. B.; Gorte, R. J.; Vohs, J. M. Evidence and Model for Strain-Driven Release of Metal Nanocatalysts from Perovskites during Exsolution. *J. Phys. Chem. Lett.* **2015**, *6*, 5106−5110.

(5) Nishihata, Y.; Mizuki, J.; Akao, T.; Tanaka, H.; Uenishi, M.; Kimura, M.; Okamoto, T.; Hamada, N. Self-Regeneration of a Pd-Perovskite Catalyst for Automotive Emissions Control. *Nature* **2002**, *418*, 164−167.

(6) Sun, Y.-F.; Li, J.-H.; Wang, M.-N.; Hua, B.; Li, J.; Luo, J.-L. A-Site Deficient Chromite Perovskite with in Situ Exsolution of Nano-Fe: A Promising Bi-Functional Catalyst Bridging the Growth of CNTs and SOFCs. *J. Mater. Chem. A* **2015**, *3*, 14625−14630.

(7) Tsekouras, G.; Neagu, D.; Irvine, J. T. S. Step-Change in High Temperature Steam Electrolysis Performance of Perovskite Oxide Cathodes with Exsolution of B-Site Dopants. *Energy Environ. Sci.* **2013**, *6*, 256−266.

(8) Carrillo, A. J.; Kim, K. J.; Hood, Z. D.; Bork, A. H.; Rupp, J. L. $La_{0.6}Sr_{0.4}Cr_{0.8}Co_{0.2}O_3$ Perovskite Decorated with Exsolved Co Nanoparticles for Stable CO_2 Splitting and Syngas Production. *ACS Appl. Energy Mater.* **2020**, *3*, 4569−4579.

(9) Zubenko, D.; Singh, S.; Rosen, B. A. Exsolution of Re-Alloy Catalysts with Enhanced Stability for Methane Dry Reforming. *Appl. Catal., B* **2017**, *209*, 711−719.

(10) Kousi, K.; Tang, C.; Metcalfe, I. S.; Neagu, D. Emergence and Future of Exsolved Materials. *Small* **2021**, *17*, No. 2006479.

(11) Zhang, J.; Gao, M.-R.; Luo, J.-L. In Situ Exsolved Metal Nanoparticles: A Smart Approach for Optimization of Catalysts. *Chem. Mater.* **2020**, *32*, 5424−5441.

(12) Neagu, D.; Tsekouras, G.; Miller, D. N.; Ménard, H.; Irvine, J. T. S. In Situ Growth of Nanoparticles through Control of Non-Stoichiometry. *Nat. Chem.* **2013**, *5*, 916−923.

(13) Neagu, D.; Oh, T.-S.; Miller, D. N.; Ménard, H.; Bukhari, S. M.; Gamble, S. R.; Gorte, R. J.; Vohs, J. M.; Irvine, J. T. S. Nano-Socketed Nickel Particles with Enhanced Coking Resistance Grown in Situ by Redox Exsolution. *Nat. Commun.* **2015**, *6*, No. 8120.

(14) Han, H.; Park, J.; Nam, S. Y.; Kim, K. J.; Choi, G. M.; Parkin, S. S. P.; Jang, H. M.; Irvine, J. T. S. Lattice Strain-Enhanced Exsolution of Nanoparticles in Thin Films. *Nat. Commun.* **2019**, *10*, No. 1471.

(15) Kim, K. J.; Han, H.; Defferriere, T.; Yoon, D.; Na, S.; Kim, S. J.; Dayaghi, A. M.; Son, J.; Oh, T.-S.; Jang, H. M.; Choi, G. M. Facet-Dependent in Situ Growth of Nanoparticles in Epitaxial Thin Films: The Role of Interfacial Energy. *J. Am. Chem. Soc.* **2019**, *141*, 7509−7517.

(16) Otto, S.-K.; Kousi, K.; Neagu, D.; Bekris, L.; Janek, J.; Metcalfe, I. S. Exsolved Nickel Nanoparticles Acting as Oxygen Storage Reservoirs and Active Sites for Redox CH4 Conversion. *ACS Appl. Energy Mater.* **2019**, *2*, 7288−7298.

(17) Spring, J.; Sediva, E.; Hood, Z. D.; Gonzalez-Rosillo, J. C.; O'Leary, W.; Kim, K. J.; Carrillo, A. J.; Rupp, J. L. M. Toward Controlling Filament Size and Location for Resistive Switches via Nanoparticle Exsolution at Oxide Interfaces. *Small* **2020**, *16*, No. 2003224.

(18) Tang, C.; Kousi, K.; Neagu, D.; Portolés, J.; Papaioannou, E. I.; Metcalfe, I. S. Towards Efficient Use of Noble Metals via Exsolution Exemplified for CO Oxidation. *Nanoscale* **2019**, *11*, 16935−16944.

(19) Kyriakou, V.; Neagu, D.; Zafeiropoulos, G.; Sharma, R. K.; Tang, C.; Kousi, K.; Metcalfe, I. S.; van de Sanden, M. C. M.; Tsampas, M. N. Symmetrical Exsolution of Rh Nanoparticles in Solid Oxide Cells for Efficient Syngas Production from Greenhouse Gases. *ACS Catal.* **2020**, *10*, 1278−1288.

(20) Gao, Y.; Lu, Z.; You, T. L.; Wang, J.; Xie, L.; He, J.; Ciucci, F. Energetics of Nanoparticle Exsolution from Perovskite Oxides. *J. Phys. Chem. Lett.* **2018**, *9*, 3772−3778.

(21) Shahid, M.; Sankarasubramanian, S.; He, C.; Ramani, V. K.; Basu, S. Ex-Solution Kinetics of Nickel-Ceria−Doped Strontium Titanate Perovskites. *Ionics* **2021**, *27*, 2527−2536.

(22) Tian, Z.; Inagaki, K.; Morikawa, Y. Density Functional Theory on the Comparison of the Pd Segregation Behavior at LaO- and FeO_2-Terminated Surfaces of $LaFe_{1-x}Pd_xO_{3-y}$. *Curr. Appl. Phys.* **2012**, *12*, S105−S109.

(23) Tian, Z.-x.; Uozumi, A.; Hamada, I.; Yanagisawa, S.; Kizaki, H.; Inagaki, K.; Morikawa, Y. First-Principles Investigation on the Segregation of Pd at $LaFe_{1-x}Pd_xO_{3-y}$ Surfaces. *Nanoscale Res. Lett.* **2013**, *8*, No. 203.

(24) Kizaki, H.; Katayama-Yoshida, H. Spinodal Nano Decomposition in Perovskite Three-Way Catalysts: First-Principles Calculations and Monte Carlo Simulations. *Chem. Phys. Lett.* **2013**, *579*, 85−89.

(25) Yanagisawa, S.; Uozumi, A.; Hamada, I.; Morikawa, Y. Search for a Self-Regenerating Perovskite Catalyst Using Ab Initio

Thermodynamics Calculations. *J. Phys. Chem. C* **2013**, *117*, 1278−1286.

(26) Hamada, I.; Uozumi, A.; Morikawa, Y.; Yanase, A.; Katayama-Yoshida, H. A Density Functional Theory Study of Self-Regenerating Catalysts LaFe$_{1−x}$M$_x$O$_{3−y}$ (M = Pd, Rh, Pt). *J. Am. Chem. Soc.* **2011**, *133*, 18506−18509.

(27) Wang, J.; Yang, J.; Opitz, A. K.; Bowman, W.; Bliem, R.; Dimitrakopoulos, G.; Nenning, A.; Waluyo, I.; Hunt, A.; Gallet, J.-J.; Yildiz, B. Tuning Point Defects by Elastic Strain Modulates Nanoparticle Exsolution on Perovskite Oxides. *Chem. Mater.* **2021**, *33*, 5021−5034.

(28) Kwon, O.; Sengodan, S.; Kim, K.; Kim, G.; Jeong, H. Y.; Shin, J.; Ju, Y.-W.; Han, J. W.; Kim, G. Exsolution Trends and Co-Segregation Aspects of Self-Grown Catalyst Nanoparticles in Perovskites. *Nat. Commun.* **2017**, *8*, No. 15967.

(29) Sun, Y.-F.; Zhang, Y.-Q.; Chen, J.; Li, J.-H.; Zhu, Y.-T.; Zeng, Y.-M.; Amirkhiz, B. S.; Li, J.; Hua, B.; Luo, J.-L. New Opportunity for in Situ Exsolution of Metallic Nanoparticles on Perovskite Parent. *Nano Lett.* **2016**, *16*, 5303−5309.

(30) Wang, Y.; Lei, X.; Zhang, Y.; Chen, F.; Liu, T. In-Situ Growth of Metallic Nanoparticles on Perovskite Parent as a Hydrogen Electrode for Solid Oxide Cells. *J. Power Sources* **2018**, *405*, 114−123.

(31) Agüero, F. N.; Beltrán, A. M.; Fernández, M. A.; Cadús, L. E. Surface Nickel Particles Generated by Exsolution from a Perovskite Structure. *J. Solid State Chem.* **2019**, *273*, 75−80.

(32) Gao, Y.; Chen, D.; Saccoccio, M.; Lu, Z.; Ciucci, F. From Material Design to Mechanism Study: Nanoscale Ni Exsolution on a Highly Active A-Site Deficient Anode Material for Solid Oxide Fuel Cells. *Nano Energy* **2016**, *27*, 499−508.

(33) Kim, K.; Koo, B.; Jo, Y.-R.; Lee, S.; Kim, J. K.; Kim, B.-J.; Jung, W.; Han, J. W. Control of Transition Metal−Oxygen Bond Strength Boosts the Redox Ex-Solution in a Perovskite Oxide Surface. *Energy Environ. Sci.* **2020**, *13*, 3404−3411.

(34) Gao, Y.; Wang, J.; Lyu, Y.-Q.; Lam, K.; Ciucci, F. In Situ Growth of Pt$_3$Ni Nanoparticles on an A-Site Deficient Perovskite with Enhanced Activity for the Oxygen Reduction Reaction. *J. Mater. Chem. A* **2017**, *5*, 6399−6404.

(35) Sun, Y.; Li, J.; Zeng, Y.; Amirkhiz, B. S.; Wang, M.; Behnamian, Y.; Luo, J. A-Site Deficient Perovskite: The Parent for in Situ Exsolution of Highly Active, Regenerable Nano-Particles as SOFC Anodes. *J. Mater. Chem. A* **2015**, *3*, 11048−11056.

(36) Mukundan, R.; Brosha, E. L.; Garzon, F. H. Sulfur Tolerant Anodes for SOFCs. *Electrochem. Solid-State Lett.* **2004**, *7*, No. A5.

(37) Choi, M.; Posadas, A. B.; Rodriguez, C. A.; O'Hara, A.; Seinige, H.; Kellock, A. J.; Frank, M. M.; Tsoi, M.; Zollner, S.; Narayanan, V.; Demkov, A. A. Structural, Optical, and Electrical Properties of Strained La-Doped SrTiO3 Films. *J. Appl. Phys.* **2014**, *116*, No. 043705.

(38) Ravichandran, J.; Siemons, W.; Scullin, M. L.; Mukerjee, S.; Huijben, M.; Moore, J. E.; Majumdar, A.; Ramesh, R. Tuning the Electronic Effective Mass in Double-Doped SrTiO 3. *Phys. Rev. B* **2011**, *83*, No. 035101.

(39) Virkar, A. V.; Chen, J.; Tanner, C. W.; Kim, J.-W. The Role of Electrode Microstructure on Activation and Concentration Polarizations in Solid Oxide Fuel Cells. *Solid State Ionics* **2000**, *131*, 189−198.

(40) Shannon, R. D. Revised Effective Ionic Radii and Systematic Studies of Interatomic Distances in Halides and Chalcogenides. *Acta Cryst. A* **1976**, *32*, 751−767.

(41) Kobayashi, S.; Ikuhara, Y.; Mizoguchi, T. Lattice Expansion and Local Lattice Distortion in Nb- and La-Doped SrTiO3 Single Crystals Investigated by x-Ray Diffraction and First-Principles Calculations. *Phys. Rev. B* **2018**, *98*, No. 134114.

(42) Guo, Y. Y.; Liu, H. M.; Yu, D. P.; Liu, J.-M. Ferroelectricity and Superparamagnetism in Sr/Ti Nonstoichiometric SrTiO$_3$. *Phys. Rev. B* **2012**, *85*, No. 104108.

(43) Glazer, A. M. Simple Ways of Determining Perovskite Structures. *Acta Crystallogr., Sect. A* **1975**, *31*, 756−762.

(44) Reuter, K.; Scheffler, M. Composition, Structure, and Stability of RuO$_2$(110) as a Function of Oxygen Pressure. *Phys. Rev. B* **2001**, *65*, No. 035406.

(45) Chase, M. W., Jr NIST-JANAF Thermochemical Tables. In *Journal of Physical and Chemical Reference Data*; American Chemical Society: Washington, DC, 1998; Vol. 9.

(46) Lee, W.; Han, J. W.; Chen, Y.; Cai, Z.; Yildiz, B. Cation Size Mismatch and Charge Interactions Drive Dopant Segregation at the Surfaces of Manganite Perovskites. *J. Am. Chem. Soc.* **2013**, *135*, 7909−7925.

(47) Schneider, C. A.; Rasband, W. S.; Eliceiri, K. W. NIH Image to ImageJ: 25 Years of Image Analysis. *Nat. Methods* **2012**, *9*, 671−675.

(48) Nečas, D.; Klapetek, P. Gwyddion: An Open-Source Software for SPM Data Analysis. *Open Phys.* **2012**, *10*, 181−188.

(49) Perdew, J. P.; Burke, K.; Ernzerhof, M. Generalized Gradient Approximation Made Simple. *Phys. Rev. Lett.* **1996**, *77*, 3865−3868.

(50) Kresse, G.; Furthmüller, J. Efficiency of Ab-Initio Total Energy Calculations for Metals and Semiconductors Using a Plane-Wave Basis Set. *Comput. Mater. Sci.* **1996**, *6*, 15−50.

(51) Kresse, G.; Hafner, J. Ab Initiomolecular Dynamics for Liquid Metals. *Phys. Rev. B* **1993**, *47*, 558−561.

(52) Kresse, G.; Hafner, J. Ab Initiomolecular-Dynamics Simulation of the Liquid-Metal−Amorphous-Semiconductor Transition in Germanium. *Phys. Rev. B* **1994**, *49*, 14251−14269.

(53) Kresse, G.; Joubert, D. From Ultrasoft Pseudopotentials to the Projector Augmented-Wave Method. *Phys. Rev. B* **1999**, *59*, 1758−1775.

(54) Blöchl, P. E. Projector Augmented-Wave Method. *Phys. Rev. B* **1994**, *50*, 17953−17979.

(55) Grimme, S.; Ehrlich, S.; Goerigk, L. Effect of the Damping Function in Dispersion Corrected Density Functional Theory. *J. Comput. Chem.* **2011**, *32*, 1456−1465.

(56) Dudarev, S. L.; Botton, G. A.; Savrasov, S. Y.; Humphreys, C. J.; Sutton, A. P. Electron-Energy-Loss Spectra and the Structural Stability of Nickel Oxide: An LSDA+U Study. *Phys. Rev. B* **1998**, *57*, 1505−1509.

(57) Wang, L.; Maxisch, T.; Ceder, G. Oxidation Energies of Transition Metal Oxides within the GGA+*U* Framework. *Phys. Rev. B* **2006**, *73*, No. 195107.

(58) Hu, Z.; Metiu, H. Choice of U for DFT+U Calculations for Titanium Oxides. *J. Phys. Chem. C* **2011**, *115*, 5841−5845.

(59) Monkhorst, H. J.; Pack, J. D. Special Points for Brillouin-Zone Integrations. *Phys. Rev. B* **1976**, *13*, 5188−5192.

(60) Towns, J.; Cockerill, T.; Dahan, M.; Foster, I.; Gaither, K.; Grimshaw, A.; Hazlewood, V.; Lathrop, S.; Lifka, D.; Peterson, G. D.; Roskies, R.; Scott, J. R.; Wilkins-Diehr, N. XSEDE: Accelerating Scientific Discovery. *Comput. Sci. Eng.* **2014**, *16*, 62−74.